The 2D-S (Stereo) Probe: Design and Preliminary Tests of a New Airborne, High-Speed, High-Resolution Particle Imaging Probe

R. PAUL LAWSON, DARREN O'CONNOR, PATRICK ZMARZLY, KIM WEAVER, BRAD BAKER, AND QIXU MO

SPEC Incorporated, Boulder, Colorado

HAFLIDI JONSSON

Center for Interdisciplinary Remotely Piloted Aircraft Studies, Office of Naval Research, Monterey, California

ABSTRACT

The design, laboratory calibrations, and flight tests of a new optical imaging instrument, the two-dimensional stereo (2D-S) probe, are presented. Two orthogonal laser beams cross in the middle of the sample volume. Custom, high-speed, 128-photodiode linear arrays and electronics produce shadowgraph images with true 10-μm pixel resolution at aircraft speeds up to 250 m s^{-1}. An overlap region is defined by the two laser beams, improving the sample volume boundaries and sizing of small ($<\sim$100 μm) particles, compared to conventional optical array probes. The stereo views of particles in the overlap region can also improve determination of three-dimensional properties of some particles.

Data collected by three research aircraft are examined and discussed. The 2D-S sees fine details of ice crystals and small water drops coexisting in mixed-phase cloud. Measurements in warm cumuli collected by the NCAR C-130 during the Rain in Cumulus over the Ocean (RICO) project provide a test bed to compare the 2D-S with 2D cloud (2D-C) and 260X probes. The 2D-S sees thousands of cloud drops $<\sim$150 μm when the 2D-C and 260X probes see few or none. The data suggest that particle images and size distributions ranging from 25 to $\sim$150 μm and collected at airspeeds $>$100 m s^{-1} by the 2D-C and 260X probes are probably (erroneously) generated from out-of-focus particles. Development of the 2D-S is in its infancy, and much work needs to be done to quantify its performance and generate software to analyze data.

1. Introduction

Reliable in situ measurements of the size, shape, and concentration of cloud particles are critical to nearly every discipline in cloud physics, including validations of remote observations of cloud radiative properties and model products. Since the early 1970s, optical imaging probes such as the two-dimensional cloud (2D-C) probe, originally developed by Particle Measuring Systems (PMS), have been used routinely on research aircraft to measure the size, shape, and concentration of cloud particles (Knollenberg 1970). The PMS instruments provided the first high-rate digital images of cloud particles and have contributed to advancements in our understanding of cloud physics. However, errors due to electro-optical limitations that are inherent in

the design of the older imaging probes have been well documented in the literature (e.g., Korolev et al. 1991, 1998; Lawson and Cormack 1995; Baumgardner and Korolev 1997; Strapp et al. 2001). Korolev et al. (1991, 1998) and Strapp et al. (2001) have shown that large counting and sizing errors occur when drops pass outside the optical depth of field (DOF). For example, a 100-μm particle can be oversized by nearly a factor of 2, undersized by a factor of 4, or missed all together (Korolev et al. 1998).

Additional counting and sizing errors occur due to the relatively slow time response of the older imaging probes, resulting from the finite time response of the photodiode array and first-stage amplifier. Baumgardner and Korolev (1997), and more recently Strapp et al. (2001) show that the time response of the 2D-C probe is limited by the time constant of the photodiode array and first-stage amplifier, leading to a significant reduction in sensitivity to particles with sizes $<\sim$100 μm at airspeeds of 120 m s^{-1} and greater. The combination of

Corresponding author address: R. Paul Lawson, SPEC Incorporated, 3022 Sterling Circle, Boulder, CO 80301.
E-mail: plawson@specinc.com

optical and electronic sizing and counting errors leads to large, potentially order-of-magnitude errors in determination of the particle size distribution (PSD) of particles $<\sim 100$ μm. In addition, the relatively coarse effective pixel size of the 2D-C probe, on the order of 25–75 μm depending on airspeed, does not provide sufficient resolution to determine the shape and phase of most particles $<\sim 300$ μm.

In this paper, we introduce a new optical imaging probe that has been designed to overcome several of the limitations of the older probes. The new probe, called a two-dimensional stereo (2D-S) probe, is designed to minimize errors associated with DOF, sample volume uncertainties, and time response. In section 2, we describe the operating principles of the 2D-S. In section 3, we show results of laboratory calibrations and tests. In section 4, we show preliminary data collected with the 2D-S installed on Learjet and C-130 research aircraft. Section 5 discusses challenges that users of the new probe will face in the development of software codes needed to reliably reject artifacts, compute PSDs, and classify crystal habits. Section 6 presents a summary and discusses recommendations for future research that the cloud physics community may consider in order to further the development of 2D-S testing and data processing.

2. 2D-S probe description and laboratory tests

A photograph of the 2D-S probe and a schematic illustrating its functional aspects are shown in Fig. 1. Two diode laser beams cross at right angles and illuminate two linear 128-photodiode arrays. The lasers are single-mode, temperature-stabilized, fiber-coupled diode lasers operating at 45 mW. The optical paths are arbitrarily labeled the "vertical" and "horizontal" probe channels, but the verticality of each channel actually depends on how the probe is oriented on an aircraft. The physical dimensions of the custom-built photodiode array are also shown in Fig. 1. The imaging optical system is based on a Keplerian telescope design having a (theoretical) primary system magnification of 5X, which results in a theoretical effective size of (42.5 μm + 15 μm)/5 = 11.5 μm. However, actual lenses and arrays have tolerances, so it is preferable to measure the actual effective pixel size by dropping several thousands of glass beads with known diameters through the object plane of the optics system. For this particular 2D-S probe, lenses were chosen to produce a 10-μm pixel size, and the glass bead tests resulted in actual pixel sizes of 9.9 μm for the horizontal channel and 9.8 μm for the vertical channel. Given the uncertainty in these measurements, we round off to an effective pixel

size of 10 μm for each channel, resulting in a sample cross section for each optical path of 0.128 cm $\times$ 6.3 cm = 0.8 cm^2, where 0.128 cm is the number of photodiodes times the pixel spacing and 6.2 cm is the distance between the arms of the probe. At 100 m s^{-1} (assuming no probe dead time and subtracting the overlap region), this results in a total sample volume of 16 L s^{-1}, which is about 3.3 times the sample volume of the PMS 2D-C probe, 4.1 times the sample volume of the PMS 260X probe, and equal to the sample volume of the Droplet Measurement Technologies (DMT) cloud imaging probe (CIP). The sample volume of the cloud particle imager (CPI), which decreases significantly with increasing particle concentration, has a maximum value that is only 4% of the 2D-S sample volume. The 2D-S laser beams define a rectangular overlap region in the middle of the probe. The 2D-S records two independent images of the same particle in the region where the beams overlap and single images of particles outside the overlap region. The spacing of particles in the direction of travel is recorded with 10-μm precision, as is the x, y position of each particle in the overlap region.

The object plane for each channel of the 2D-S imaging systems is at the midpoint between the respective sample arms. Particles are in focus at the object plane and are detectable up to a distance away from the object plane depending on particle size. We define the distance away from the object plane where a particle's shadow is still detectable on the photodiode array at the 50% threshold level as DOF$_{50\%}$. The relationship for DOF$_{50\%}$ of a circular opaque particle is a function of the square of particle radius (r) and the wavelength of the laser beam (λ). Knollenberg (1970) and others have found that the form of this relationship is

$$\text{DOF}_{50\%} = \pm cr^2/\lambda. \tag{1}$$

The constant c can be determined theoretically from diffraction theory or experimentally (Lawson and Cormack 1995; Korolev et al. 1991, 1998) for a particular electro-optical system by positioning circular objects of known size at measured distances from the object plane and recording the resulting images. For the 2D-S, c was determined theoretically using a ZEMAX software code (available online at www.zemax.com) to have a value of 8. However, this does not include the effect of discrete pixels, and the actual value could be closer to 6, which is a value that is commonly used and is close to the average based on measurements found in the PMS 2D-C operators' manual. For the sake of example, assuming that $c = 8$ in (1), the value of DOF$_{50\%}$ for $\lambda =$ 0.8 and a particle with a diameter $d = 16$ μm, is ± 0.64 mm, which is the maximum distance a particle can be
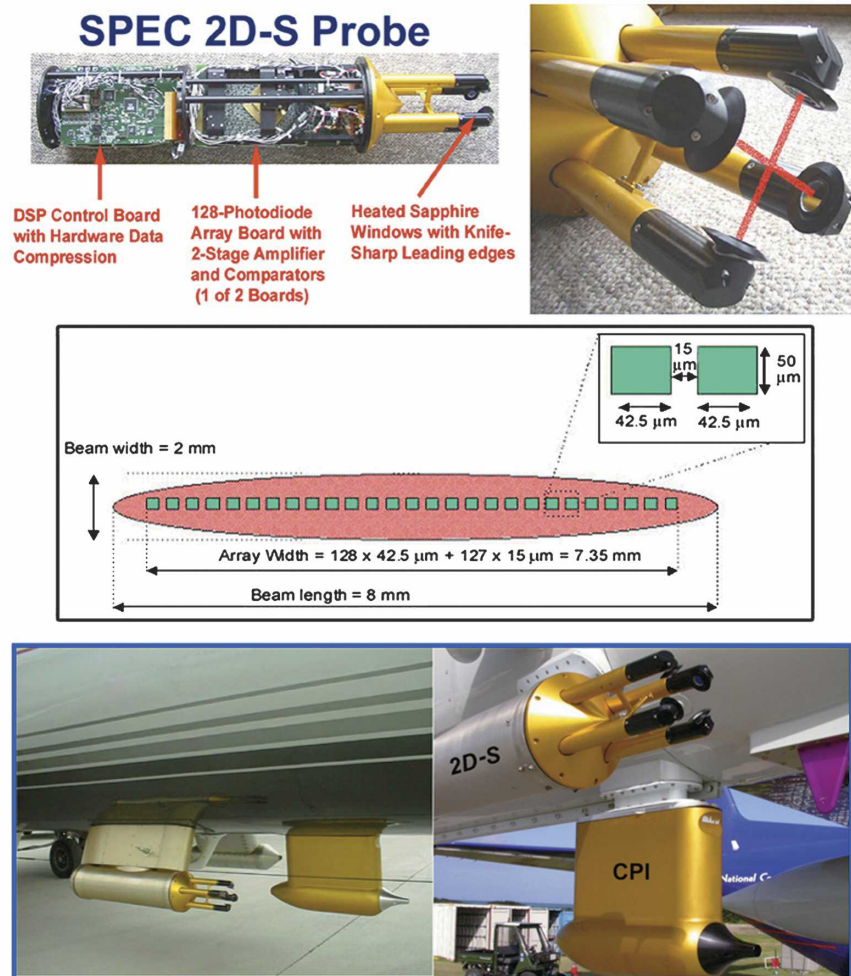
FIG. 1. Photographs showing (top left) some principal features of the 2D-S probe, (top right) a close up of the sample region with crossed laser beams, (middle) a drawing showing the geometry of the linear 128-photodiode array where the shaded oval area represents the laser beam, and (bottom) photographs of the 2D-S probe installed on (lower left) the SPEC Learjet and (lower right) NCAR C-130.

displaced from the object plane and still remain in the overlap region of the two laser beams. Particles with $d < \approx 16$ μm then have a $DOF_{50\%}$ that falls within the overlap region, and particles with $d > \approx 16$ μm have a $DOF_{50\%}$ that falls outside the overlap region.

As shown schematically in Fig. 2, the position of all particles that fall within the overlap region of the two laser beams is recorded, so the distance of each of these particles to the object plane of each optical path is also known. As shown in Fig. 3, as a spherical particle is moved away from the object plane, its image becomes donut-shaped and systematically increases in maximum dimension until it starts to fragment into discrete pixels and finally disappears all together. A "particle event" (i.e., a count) occurs when the shadow depth of any pixel is $\geq$50% of the background light level and termi-

nates when one 128-photodiode slice is all zeros (i.e., no occulted photodiodes). Since the distance to the object plane is recorded for all particles that fall within the 2D-S overlap region, corrections for depth-of-field and sample volume effects can be applied to improve measurements of particle concentration. In addition, the improved pixel resolution and time response make it possible to correct the size of out-of-focus (i.e., "donut") images, whether they are in or outside the overlap region. Techniques such as described by Korolev et al. (1998) can be used to estimate the actual diameters of spherical particles from their diffracted images.

Figure 2 also shows that very small particles ($< \approx 16$ μm) that are outside the overlap region generate a shadow depth that is too shallow to exceed the threshold level and are therefore not detected. This is impor-
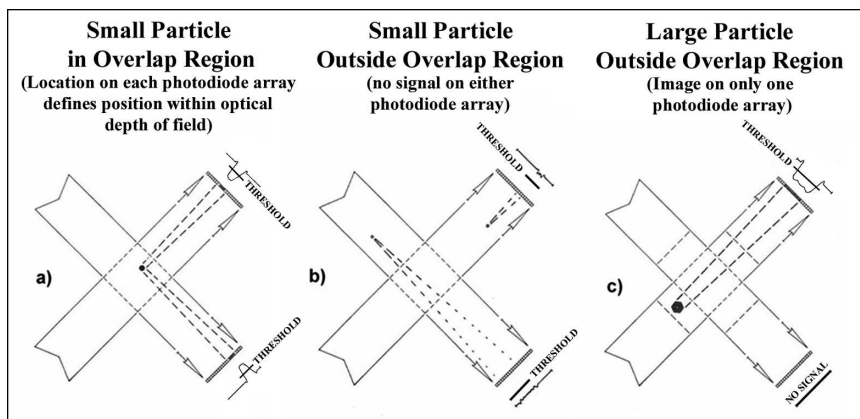
FIG. 2. Schematic drawings showing crossed laser beams (bounded by arrowheads), square overlap region in the middle of the two beams, 128-photodiode arrays at the end of the arrowheads, shadow width of sampled particle, and intensity of shadow as seen by the photodiode arrays. Examples are shown for (a) very small particle in overlap region, (b) very small particle outside overlap region, and (c) large particle outside overlap region.

tant because, otherwise, high concentrations of small particles would still cause triggering due to coincidence in the regions where the laser beams do not overlap. Particles $<\approx 110$ μm will have a $DOF_{50\%}$ that is variable according to (1) and may or may not produce detectable shadows, while particles $>\approx 110$ μm will produce detectable shadows everywhere in the sample volumes. This is because the $DOF_{50\%}$ of particles $>\approx 110$ μm is greater than the distance between the sample arms, which is 6.5 cm. Since larger particles are found in lower concentrations, the probability is low that two larger particles will pass simultaneously through the nonoverlap regions of the laser beams, producing a false stereo event. Each particle's transit time is measured and used along with their arrival time on each channel to identify "stereo" particles, that is, particles with two independent images. Therefore, if a large particle passes outside the overlap region and a small particle arrives at the same time within the overlap region, these particles may be considered as separate particles.

If only the overlap region is used to determine particle concentration, the resulting sample volume (0.128 cm × 0.128 cm × true airspeed) equals 0.16 L s^{-1} at an airspeed of 100 m s^{-1}, which is about 3 times the sample volume of the forward scattering spectrometer probe (FSSP) (Knollenberg 1981). If particle concentration and particle size distributions are determined from only particles in the overlap region, the sample volume is significantly smaller than when the entire length of each optical channel is used. On the other hand, if particles <16 μm are counted and sized only in the overlap region, but the entire available optical sample path of each channel is used for the remaining particles, some

of the particle images from about 16 to 110 μm will contain counting and sizing uncertainties. However, with the 2D-S, corrections to DOF and thus sample volume can be made based on size corrections of the diffraction patterns of each image (Korolev et al. 1998). The optimal selection of what sizes of particles in the final computed size distribution is drawn from only particles in the overlap region, with the remaining larger particles being counted and sized outside the overlap region, depends on the particle size distribution itself. This is a problem that will require additional work to optimize.

To substantially increase the time response of the photodiode array and first-stage amplifier, a new custom-built, 128-element linear photodiode array was built by CentroVision Corporation. Instead of the 200-μm elements in photodiode arrays used in conventional imaging probes, each photodiode in the 2D-S array is 42.5×50 μm (Fig. 1), thereby reducing capacitance and increasing speed. The dimensions of the 128-photodiode array chip are positioned on a 12-layer printed circuit board that is specially designed to reduce lead length and increase speed. The time responses of the 2D-S and 2D-C probes were tested in the laboratory using a laser light pulse with a 5-ns fall time (to simulate a particle occulting the laser beam on a photodiode). The 2D-C has a $(1/\varepsilon)$ response time constant of 760 ns, while the 2D-S probe has a response of 41 ns, which is nearly 20 times faster than the 2D-C probe. However, the 2D-C probe tested was an older version, and some newer probes may have slightly faster response times. For example, Strapp et al. (2001) report an average time constant of 600 ns, and Gayet et al.
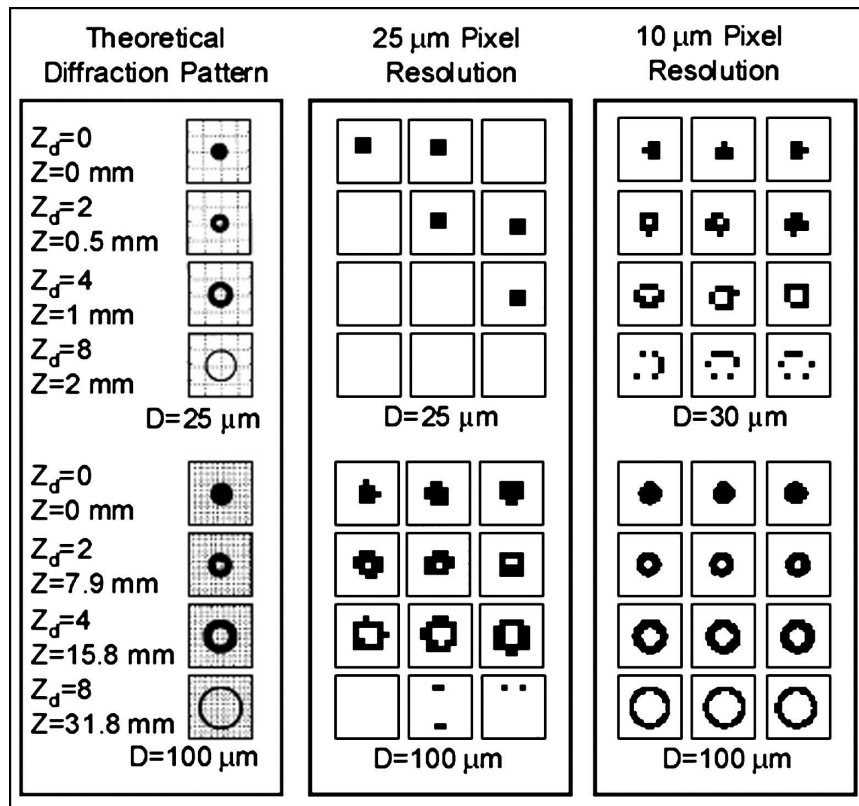
FIG. 3. Simulations of (left) theoretical diffraction pattern with infinite pixel resolution, (middle) for 25-μm pixel resolution, and (right) for 10-μm pixel resolution. Out-of-focus diffraction patterns are shown as a function of actual (Z in mm) and nondimensional distance from the object plane ($Z_d = 4Z\lambda/D^2$, where D is disc diameter and λ is wavelength of laser light). Diffraction patterns assume ideal instrument optics and time response (i.e., no degradation in image quality due to optics or instrument time response). Adapted from Korolev et al. (1998) and Korolev (2005).

(1993) reported a time constant of 280 ns for one probe.

An additional test that evaluates the response time of the 2D-S was conducted by Dr. Dagmar Nagel with a unique high-speed spinning glass fiber calibration unit developed and operated by the Institute for Coastal Research (GKSS). The 2D-S probe imaged an 8-μm glass fiber spinning at 233 m s^{-1}. In comparison, using the same GKSS spinning-fiber setup, the fastest response that the PMS 2D-C and DMT CIP[1] probes achieved was to image a 75-μm glass fiber at 75 m s^{-1}.

---

[1] Subsequent to the acceptance of this paper, some of the DMT CIP probes have been modified with a new photodiode array that appears to significantly improve the time response. The CIP measurements shown in this paper reflect the older CIP technology. There has not been an evaluation of the time response of new CIP technology; DMT anticipates that this will be presented in a subsequent publication (D. Baumgardner 2006, personal communication).

A 12-layer printed circuit board with a 32-bit ADSP-2191 digital signal processor (DSP) running at 150 MHz controls very large, ball-grid array complex programmable logic devices (CPLDs) that perform hardware data compression to handle the extremely high data rates (Fig. 1). The 2D-S probe outputs data at a maximum rate of 17 million samples per second per 128-photodiode array. This amounts to a maximum "raw" data rate of 1.1 Gbyte s^{-1}. Hardware data compression reduces the data rate by up to a factor of 8 (depending on particle size and concentration). Data from the prototype 2D-S probe were transferred using an off-the-shelf high-level data link control (HDLC) high-speed serial PCI interface card; thus existing aircraft wiring from conventional 2D imaging probes could be utilized. Using the prototype 2D-S, compressed data are recorded up to rates of 4 Mbit s^{-1}, resulting in a maximum dead time of 0.25 s, which only occurs when the probe encounters high ($>\approx 100$ cm^{-3}) particle concen-

trations. Future modifications now include using a 100 Base-T Ethernet interface, which has a theoretical maximum data transfer rate of 100 Mbit s^{-1}. However, the maximum data rate is currently limited by the 2D-S DSP, which can transfer data at rates up to 37 Mbit s^{-1}. Upgrading to a faster DSP in the future could lead to data rates that approach the theoretical maximum of 100 Mbit s^{-1}. The Ethernet interface will increase the existing 2D-S probe maximum data rate and decrease dead time by about a factor of 10 and can be supported by a laptop computer in place of the desktop used in the prototype.

The DSP and CPLDs control all probe housekeeping functions, including laser intensity, internal temperature, anti-icing heaters, timing, image diagnostics, and data transfer. Each particle is time-stamped so that stereo pairs can be identified using time of occurrence and transit time. Because the 2D-S uses a 128-photodiode array with 10-μm resolution, the probability of a photodiode being continuously occulted, due to optical contamination or electronic noise, is much greater than with probes that have 32 photodiodes and 25-μm pixels. For this reason, the DSP monitors each photodiode to determine if it is being continuously set and, if it is, a "bit mask" is set that disables the response of the "stuck bits." A user can also opt to mask bits by inputting information from the data system computer. As shown in Fig. 1, the 2D-S probe is designed with nonwetting, heated sapphire windows that have a knife-sharp leading edge to minimize particle bounce and breakup, which is suspected to produce artifacts that cause errors in imaging probes (Jensen and Granek 2002).

3. Results of preliminary flight tests

The 2D-S probe was installed on the SPEC, Inc., Learjet and flown on seven research flights during November–December 2003 and eight flights during April–May 2004. In November 2004, it was installed on the National Center for Atmospheric Research (NCAR) C-130 aircraft for the Rain in Cumulus over the Ocean (RICO) project. Data were collected by the Learjet in cirrus clouds, wave clouds, and upslope clouds along the Front Range of the Rocky Mountains in Colorado. Data were collected by the C-130 in an upslope cloud along the Front Range and on 13 missions in warm cumulus clouds near Antigua during the RICO project. Figure 1 shows photographs of the 2D-S probe installed on the Learjet and the NCAR C-130. The 2D-S probe is installed in such a way on both aircraft that the optical channels are not actually oriented vertically and horizontally. Instead, on the Learjet, the channels are rotated by about 30°, and on the C-130 they are rotated

by about 45°. Since on both aircraft the 2D-S probe protrudes from an axially symmetric body (i.e., the wing pod on the C-130 and the Learjet fuselage), particles may be experiencing a radial trajectory as they pass through the sample volume of the probe. This produces a slight skewness in the appearance of the images, which would be especially noticeable in (spherical) water drop images, as seen later in section 3c. This aberration can be corrected in software, but no attempt to do so has been done in the 2D-S images shown in this paper.

Here we present comparisons of 2D-S images with images collected using a cloud particle imager and conventional imaging probes installed on the research aircraft. The 2D-S results are based on preliminary software programs. Because the analysis software is preliminary, we opt to show only particle counts in all cases except one, which is when the probe was in small drizzle drops during RICO. In the RICO case, we incorporated recent work by Korolev (2005) to correct for out-of-focus images, and also, because the drops are small ($\leq$150 μm), we believe that artifacts that may be generated from drop shattering and/or incomplete diffraction rings are minimal. The development of mature software capable of automatically rejecting artifacts (e.g., images fragmented from large particles shattering on the probe tips), accurately determining stereo particles, sizing corrections to nonspherical particles, and improving image-to-volume algorithms, is a work in progress.

a. Mixed-phase upslope and wave clouds

Figure 4 shows examples of 2D-S, CPI, and 2D-C particle images collected at –13°C by the NCAR C-130 in a mixed-phase upslope cloud east of the Colorado Front Range. The 10-μm resolution, 0.128-cm width of the sample area and high-speed response of the 2D-S probe allow it to show ice particles within a field of small cloud droplets. Compared to the 2D-C particle images, the 2D-S shows considerably more detail of ice crystal structure. Figure 4 also shows examples of "stereo" views of images that passed through the overlap region of the 2D-S probe. The stereo views reveal details of the three-dimensional structure of particles that cannot be determined from a single shadow image of the particle.

Figure 5 shows an example of measurements from the SPEC Learjet during penetration of a wave cloud that formed over the Colorado Front Range. The evolution of particles is shown starting from the top of the figure, which is the leading (western) edge of the wave cloud. The wave cloud undergoes the expected particle evolution at −27°C (Baker and Lawson 2006), that is, a
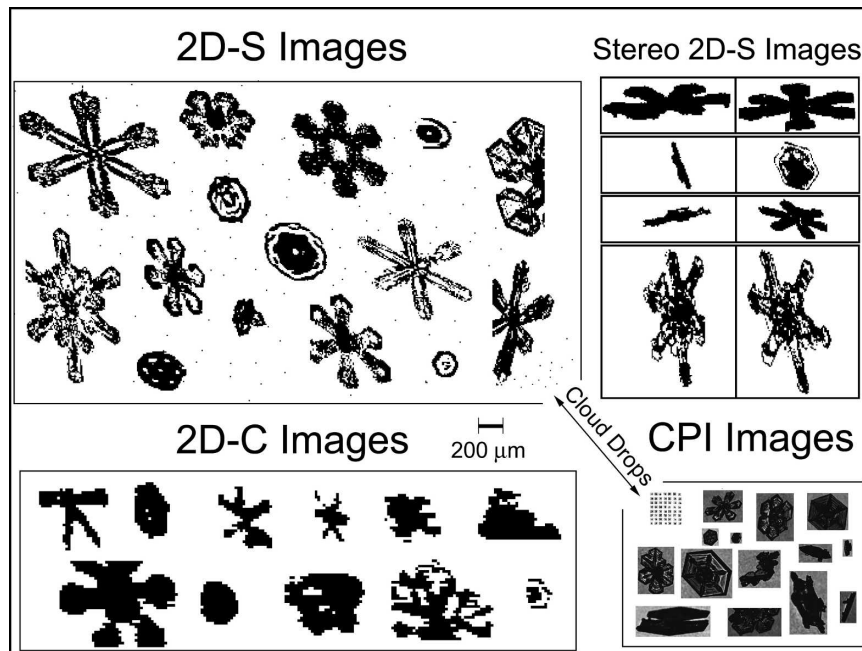
FIG. 4. Examples of images from the 2D-S, CPI, and 2D-C probes in a mixed-phase upslope cloud investigated by the NCAR C-130 research aircraft. (All of the particle images in this figure have been hand-picked and placed using a graphics tool; i.e., the spatial relationships of the particles are not as observed by the probes.)

transition from supercooled cloud droplets near the leading edge, changing to a mixed-phase region, which rapidly turns into glaciated cloud. The cloud drop size distribution from an FSSP is displayed at the left of the figure, showing that the size of the supercooled drops ranges from about 4 to 18 μm in diameter, with a mean diameter of 11.6 μm. Both the CPI and the 2D-S probes detect the cloud drops, as seen in the sample images. The location of the first ice particles encountered in the mixed-phase cloud region is of interest to cloud physicists, because this relates to ice nucleation, a process that is still poorly understood in wave clouds (Baker and Lawson 2006). The data in Fig. 5 show that the 2D-S detects ice particles much closer to the cloud leading edge than either the CPI or the 2D-C probes. The 2D-C does not detect particles with sizes $<\sim$100 μm because of the slow response of the photodiode array and front-end amplifier. (Later in this section, we show additional probe comparisons from the RICO project that support this statement.) The CPI easily sees the cloud drops, but since the imaging laser is triggered, the probe response is dominated by the high concentration of drops, so it is often inactive when larger (ice) particles enter the sample volume. The ability of the 2D-S to detect small ice "earlier" into the traverse of the wave cloud may provide the basis for a better understanding of the ice nucleation process in clouds.

b. Cold wave and cirrus (ice) clouds

Figure 6 shows examples of small spheroidal particles and budding rosettes in a cold ($-45°$C) cirrus cloud. The figure is configured to show the transition from a region of small particles to budding rosettes and highlights how the 2D-S probe sees these particles and the 2D-C barely responds. This is emphasized by the total particle count, where the 2D-S recorded 268 897 particles compared with 264 particles seen by the 2D-C over a 40-s time period. Also, the shapes of many of the larger ($>\sim$100 μm) budding rosettes, which are confirmed by the CPI images, are discernable and can be identified as rosettes in the 2D-S imagery, whereas the 2D-C sees only 1–5 pixel images whose shape is indistinguishable. Figure 7 shows another example of small ice particles and budding rosettes in a cold ($-50°$C) cirrus cloud. In this figure, six 2D-S image strips have been aligned horizontally. Notable in this figure is the large number of small ice particles in the absence of large particles that could have shattered on the probe tips. Observations of high concentrations of small ice particles in cirrus have been reported by some investigators (Lawson et al. 2001; Gayet et al. 2002; Lawson et al. 2006) but questioned by others as being a possible result of crystal shattering. The 2D-S probe may shed new light on this issue.
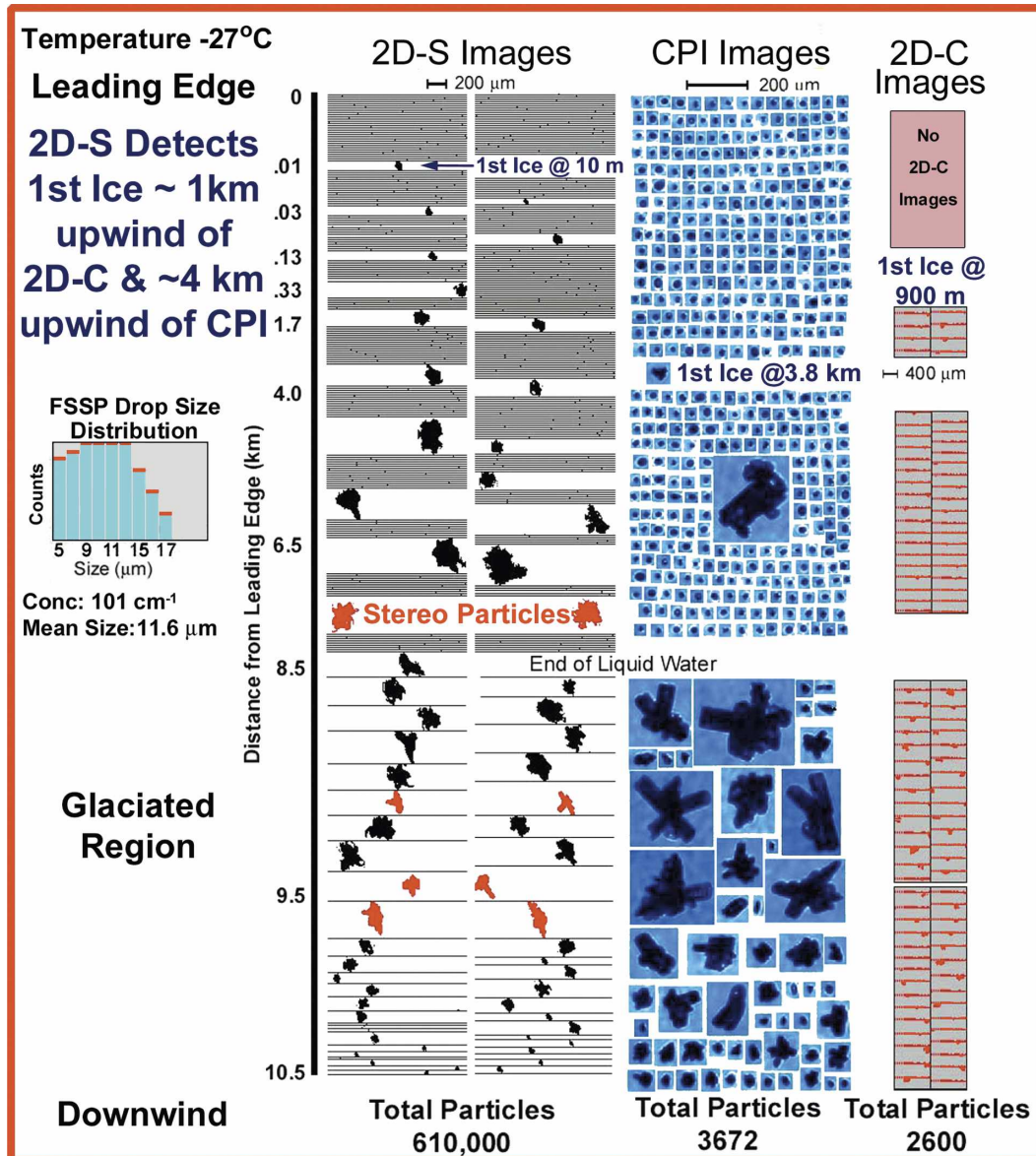
FIG. 5. Examples of 2D-S, CPI, and 2D-C particle images observed starting from (top of figure) the leading edge of a wave cloud containing supercooled drops, extending into the mixed-phase region and terminating (bottom of figure) in the glaciated region. The FSSP cloud drop distribution near the leading edge is shown at the left. Examples of 2D-S stereo images are shown in red.

Figure 8 shows image data from several particle imaging probes on the SPEC Learjet and WB-57 research aircraft, operated by the National Aeronautics and Space Administration (NASA). Both aircraft participated in the Middle Latitude Cirrus Experiment (MidCiX) and flew a coordinated mission in a system of persistent, vertically stacked wave clouds. The wave cloud system was located over the Colorado Front Range and had a cloud-base temperature of –43°C and a cloud-top temperature of –63°C. A Rosemount icing

probe (Mazin et al. 2001; Cober et al. 2001) indicated that there was no detectable supercooled liquid water drops in these clouds.

Figure 8 shows portions of the Learjet and WB-57 flight tracks as they penetrated the same wave cloud, based on video records and flight notes from both aircraft. The Learjet penetrated the cloud at 10.6 km (–54°C), and the WB-57 penetrated 200 m lower in the cloud, at –53°C. Both aircraft carried CPIs and 2D-C-type imaging probes. The 2D-C probe on the Learjet
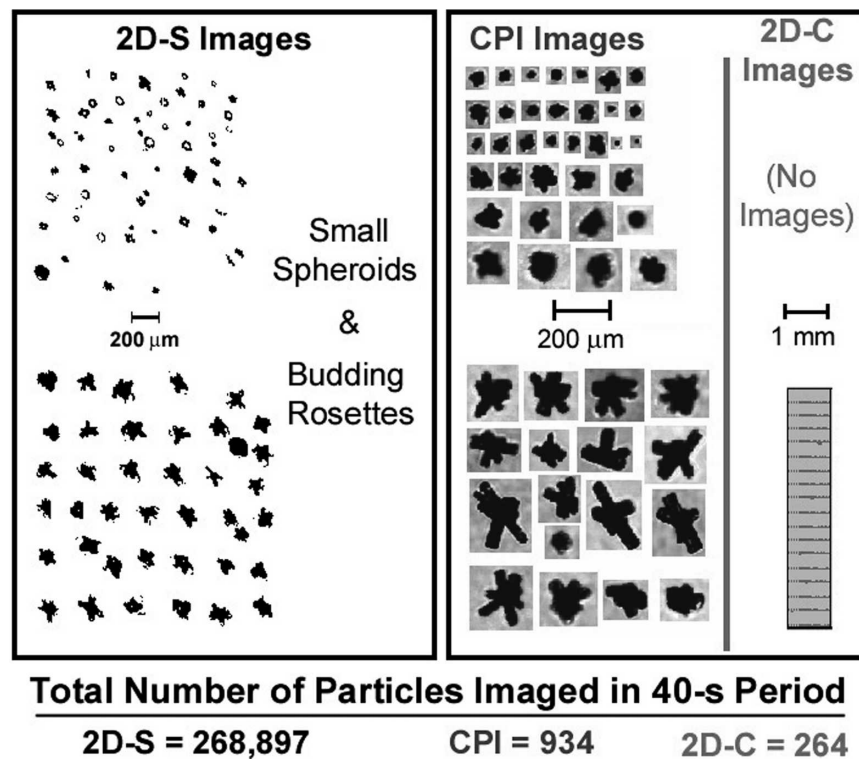
FIG. 6. Examples of images from the 2D-S, CPI, and 2D-C probes in a cirrus cloud ($-45°$C) investigated by the SPEC Learjet.

was manufactured by PMS. The WB-57 flew a DMT cloud, aerosol, and precipitation spectrometer (CAPS) probe (Baumgardner et al. 2001), which is a composite of probes, one of which is a DMT CIP. The CPI particle images in Fig. 8 show that both aircraft penetrated regions with small spheroidal particles and budding rosettes (i.e., rosettes with short branches). The maximum dimension of the budding rosettes observed by the
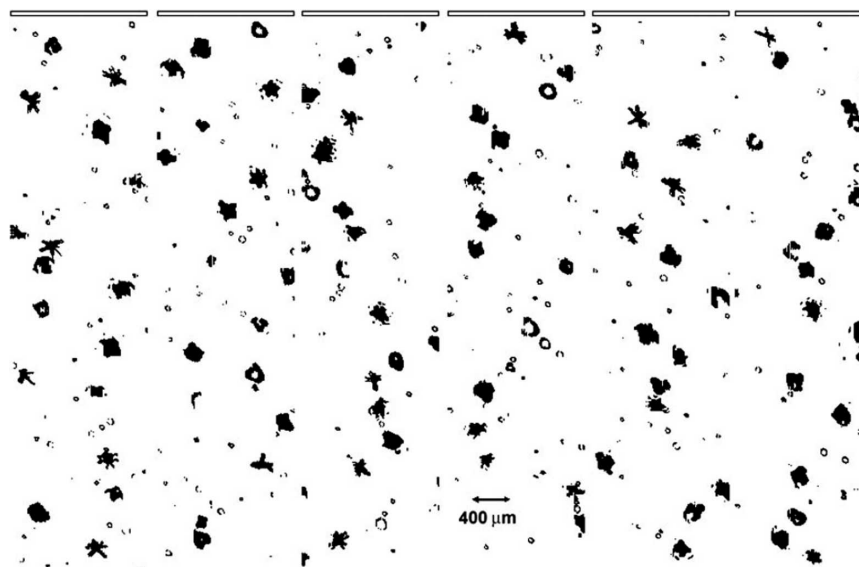

FIG. 7. Example of images of budding rosettes, irregular-shaped particles, and small particles recorded by the 2D-S during a flight in a thin cirrus cloud at –50°C.
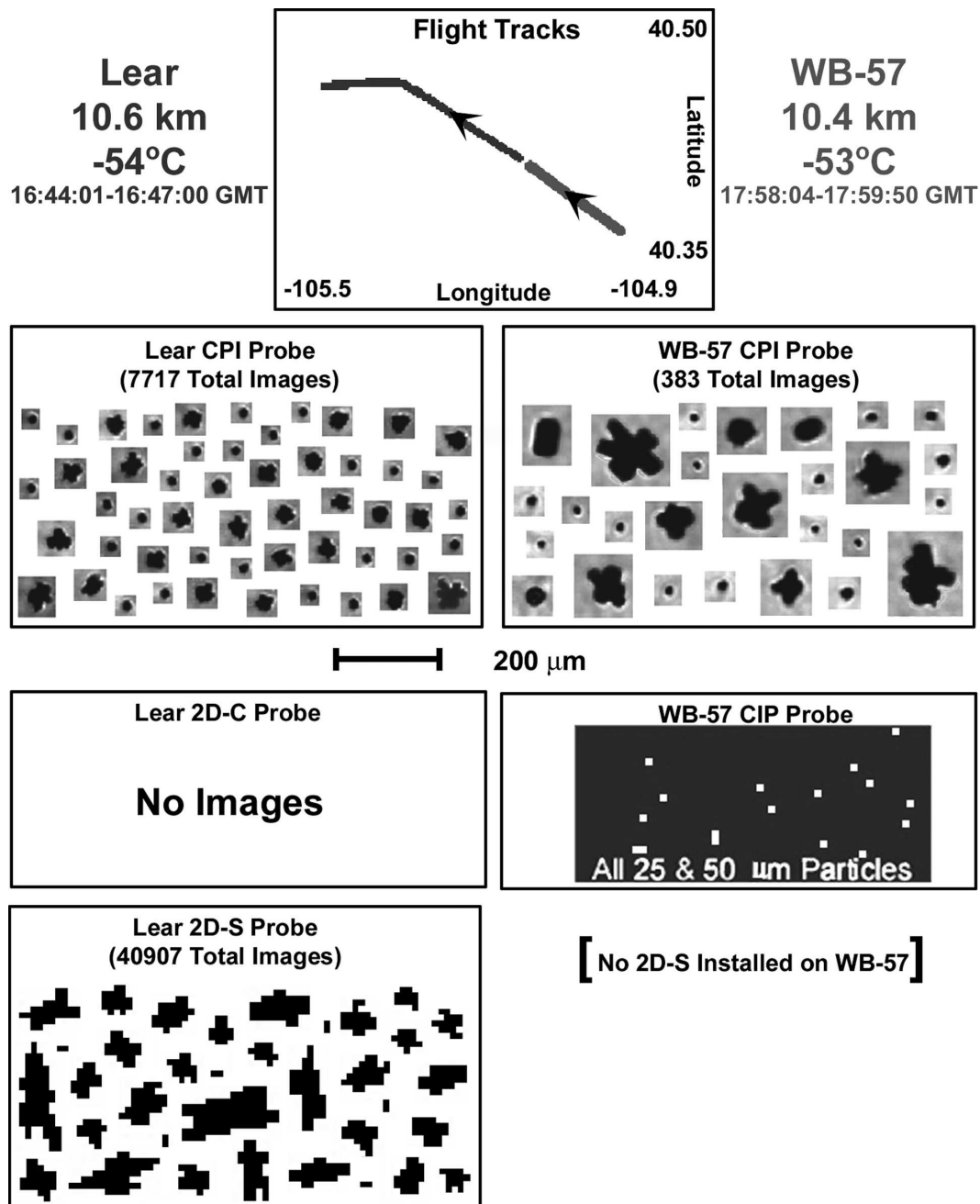
FIG. 8. Comparison of particle images from various probes installed on the SPEC Learjet and NASA WB-57 in a cold wave cloud where the two aircraft penetrated the same region of cloud.

Learjet is about 75 μm, while the WB-57 recorded some slightly larger particles, with maximum dimension of about 125 μm, during its penetration 200 m lower in the cloud. Of note is the observation that during the entire penetration (and actually during the entire flight), there were no particle images recorded by the Learjet PMS 2D-C probe. The DMT CIP probe, on the other hand, only recorded images that were 25 and 50 μm (one and two pixels). The true airspeed of each aircraft during the cloud penetrations was about 160 m s^{-1}. Since the CPI imaged particles up to 125 μm at the same time that the CIP recorded 25- and 50-μm images, it would appear that the front-end electro-optics of the CIP were not fast enough to capture the entire particle image. Figure 8 shows that the 2D-S probe recorded particle images as small as 10 μm and with the largest image
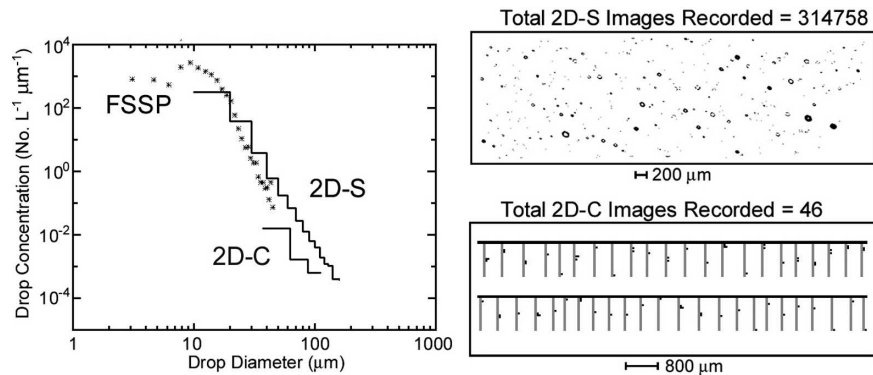
Fig. 9. Comparisons of (left) PSDs from FSSP, 2D-S, and 2D-C and (right) droplet images for the time period 1853:40–1857:50 UTC 7 Jan 2005.

dimension being 200 μm during the penetration. However, since the 2D-S electro-optics are fast enough to accurately capture the image, it is possible that the 200-μm images are out-of-focus particles that are actually about 125 μm in size (see Korolev et al. 1998).

c. Warm cumulus (water) clouds

The RICO project addressed several aspects of the warm rain process, one of which is evolution of the droplet spectra in small, warm cumulus clouds (Rauber et al. 2003, personal communication). The 2D-S probe can detect and size drops from 10 μm to >1 mm in diameter, so it is capable of measuring the evolution of the drop size distribution in the critical size region where cloud drops coalesce into drizzle and eventually become raindrops. Measurements of the drop size distribution in warm cumulus have been made during several previous projects using PMS 2D-C and 260X probes (e.g., Blyth et al. 2003; Jensen and Granek 2002). We show here that these instruments appear to have improperly measured the critical size range of drops with diameters from about 25 to 150 μm.

Figure 9 shows examples of 2D-S and 2D-C images, along with PSDs from the FSSP, 2D-S, and 2D-C during a 250-s penetration in a cloud region on 7 January 2005. During this time period, the C-130 encountered cloud and drizzle drops that produced in-focus 2D-S images that extended out to 150 μm in diameter. The FSSP and 2D-C data were processed using standard NCAR processing software (NCAR 2003). The 2D-C depth-of-field correction for sample volume comes from the PMS 2D-C manual (NCAR 2003), which uses a value of $c \approx 6$ in (1). The 2D-S images are shown exactly as they were recorded. Based on theory shown in Korolev et al. (1998) and algorithmic simulations recently developed for SPEC by Korolev (2005), out-of-focus 2D-S images (i.e., "donuts") with maximum

dimensions $\geq$30 μm were automatically resized. The Korolev (2005) algorithm uses the ratio D_{area}/D_{max}, where D_{area} and D_{max} are explained in detail in Korolev et al. (1998).[2] The Korolev (2005) algorithm is only applied to the portion of the 2D-S PSD $\geq$30 μm because smaller images do not contain enough information (e.g., Poisson spot) to reconstruct the original particle size. The concentration of 2D-S images $\leq$20 μm was adjusted using depth-of-field and sample-volume corrections based on (1) with a value of $c = 8$, which was determined from laboratory calibrations with glass beads. No attempt was made to eliminate artifacts; however, in the RICO PSD presented here, there is little evidence of drop shattering or other artifacts. Also, the occurrence of images "joined together" is minimal and can be ignored.

2D-C images from 50 to 150 μm (two to six pixels) cannot be resized because of the poorer instrument response time and pixel resolution (i.e., no Poisson spot; see Fig. 3). The 2D-C drop size distribution was computed using depth-of-field corrections published in the PMS 2D-C manual. As shown in Table 1, the 2D-C recorded a total of 46 images, while the 2D-S horizontal channel recorded 314 758 images during the same 250-s time period; 90 of the 2D-S images had diameters of 100 μm or greater. A comparison of the number of particles in Fig. 9 shows that the 2D-C recorded about 0.1% of the particles seen by the 2D-S in the size range from about 30 to 150 μm, and the 2D-C PSD was about an order of magnitude lower than the 2D-S in this size range.

Of the total images recorded by the 2D-S, 30 of the images had diameters >100 μm, and the 2D-C probe

---

[2] The algorithm developed by Korolev (2005), which can be viewed online at www.specinc.com, will be the subject of a future paper by Korolev and coauthors (Korolev 2006).

TABLE 1. Comparison showing response of 2D-S probe horizontal (H channel) with expected counts from 2D-C probe assuming theoretical instantaneous time response and actual counts for time period with maximum drop diameter of (left) 150 μm and (right) maximum drop diameter of 120 μm. The data shown at left are from RICO for the 250-s time period from 1853:40 to 1857:50 UTC 7 Jan 2005, and the data shown at right are a continuous 65-s time period within the 250-s time period.

Maximum drop size = 150 μm				
2D-S size (μm)	H-channel 2D-S counts	2D-C size (μm)	Expected 2D-C counts	Actual 2D-C counts
10	181 273			
20	95 271	25	89 357	0
30	27 989			
40	6075			
50	1992	50	3969	30
60	1166			
70	469	75	595	9
80	326			
90	106			
100	60	100	82	7
110	19			
120	8	125	8	0
130	3			
140	0			
150	1	150	0.5	0
160	0			
Maximum drop size = 120 μm				
2D-S size (μm)	H-channel 2D-S counts	2D-C size (μm)	Expected 2D-C counts	Actual 2D-C counts
10	30 876			
20	18 564	25	16 585	0
30	4508			
40	895			
50	326	50	622	0
60	222			
70	74	75	97	0
80	48			
90	19			
100	9	100	13	0
110	2			
120	1	125	0.8	0
130	0			

did not record any images >100 μm. Therefore, even though a single channel of the 2D-S has 1.75 times the sample volume of the 2D-C for drops <150 μm, the absence of recorded 2D-C images >100 μm cannot be explained by sampling statistics (Table 1). The 260X probe recorded only six drops during the same 250-s time period.

The 2D-C probe did not record any images larger than 100 μm in diameter during the 250-s period, which suggests that the few images it did record may actually have been out-of-focus images of larger (100–150 μm) drops. This is supported by the data shown in Table 1, which shows the 2D-S horizontal (H) channel counts per bin for 65 s during the 250-s period when the 2D-C did not record any images. During this 65-s period, the 2D-S probe H channel recorded 55 544 drop images, 375 with diameters from 60 to 120 μm and 12 with diameters 100 μm and larger. Since the 2D-C probe did not record any images, this suggests that the threshold

drop size that the 2D-C probe detected was about >100 μm at the 103 m s^{-1} airspeed of the C-130. With this information, we can hypothesize that the images recorded by the 2D-C in the 50–100-μm size bins during the 250-s time period (Fig. 9) are actually drops in the size range from 100 to 150 μm that produce smaller images due to inadequate time response of the probe.

Another interesting observation drawn from Fig. 9 is that if one extrapolates the PSD from the FSSP to the 2D-C, they form a relatively straight line, implying that the 2D-C PSD is reasonable. Given that it is likely that the 2D-C is recording measurements in the 25–100-μm size range that are actually out-of-focus images of larger drops, one can draw the conclusion that many of the PSDs previously reported in this size range are erroneous. To be more specific, measurements from the 2D-C with time constants similar to the NCAR instrument, when operated at 100 m s^{-1} or faster, likely do not detect (spherical water) particles with sizes <100
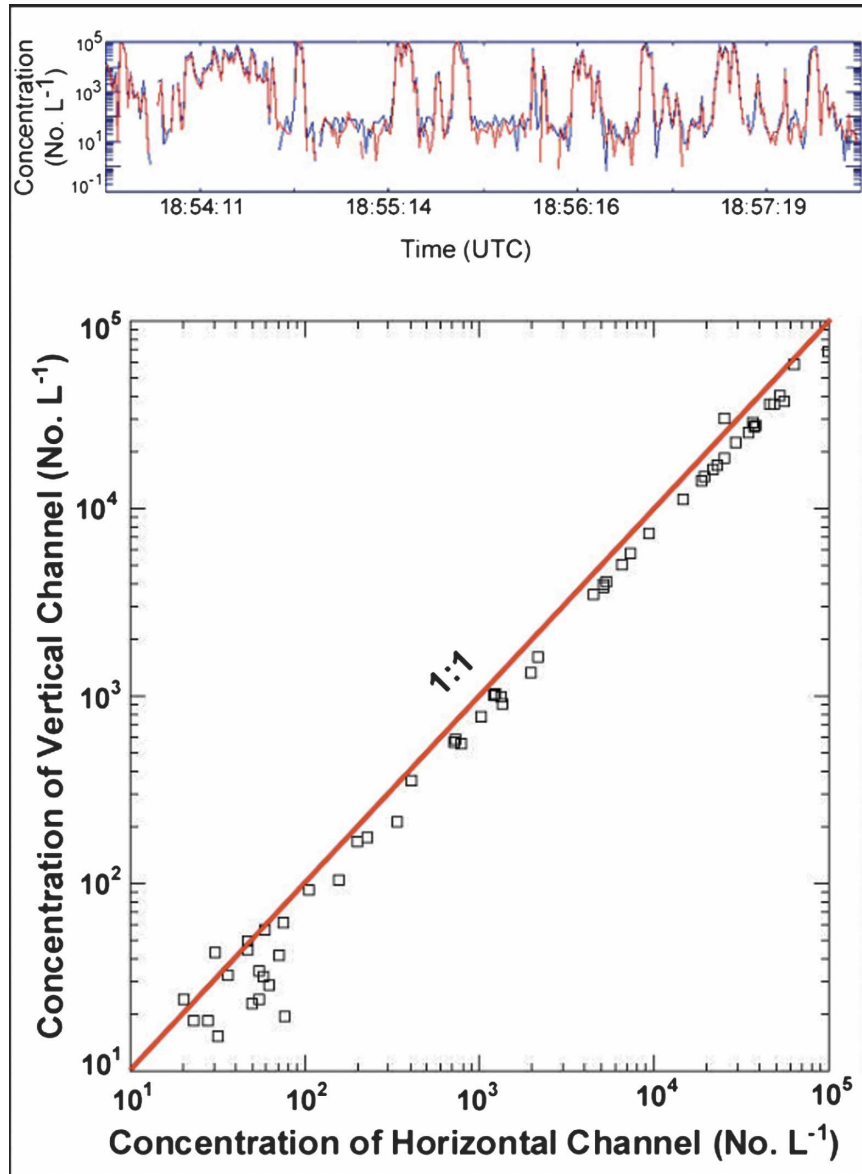
FIG. 10. Comparison of (top) time series data and (bottom) a scatterplot for the "vertical" and "horizontal" channels of the 2D-S probe. Occasional data dropouts in the time series are when a channel is in overload. Each square in the scatterplot is a 4-s average. Measurements are for the cloud penetration from 1853:40 to 1857:50 UTC 7 Jan 2005.

μm. If particles >100 μm are present, the out-of-focus images from these particles may artificially create a pseudo-PSD from 25 to 100 μm.

A comparison of measurements from the (independent) vertical and horizontal 2D-S channels is similar to comparing the response to two independent imaging probes. Previous efforts to compare the output from several 2D-C imaging probes installed on the same aircraft have shown that errors in concentration of up to 50% are expected (Gayet et al. 1993). Drop size distri-

butions and time series of drop concentration from both the vertical and horizontal 2D-S imaging channels are shown in Fig. 10. The good agreement in the time series of drop concentrations between the vertical and horizontal channels is encouraging. This level of agreement is not always present in the RICO dataset, because the functioning of one channel or the other is sometimes degraded in the salty tropical environment because of window contaminants and/or optical alignment issues.

4. Challenges presented by 2D-S imaging

While the 2D-S provides a fresh new look at cloud particles, its high resolution and fast time response introduce data-processing challenges that were often smeared or hidden by the poorer response of the older imaging probes. For example, Fig. 11 shows examples of 2D-S particle images that have "holes" in them because they are out of focus and/or are due to light transmission through the crystal. To better understand the effects of imaging particles that are out of focus, we replaced one of the 2D-S linear arrays with a digital camera and made images of glass beads at various distances from the object plane (Fig. 11b). Next, using software we averaged the 2.3-μm pixels of the digital camera to correspond with the 10-μm pixel resolution of the 2D-S. The actual 2D-S images (Fig. 11a) compare very well with the images of out-of-focus glass beads shown in Fig. 11b, suggesting that the donut images are likely out-of-focus spherical particles (see Fig. 3). Since the pixel resolution and time response of the 2D-S is very good, it is possible to make reliable corrections to the sizes of these particles.

Another factor that may affect the quality of 2D-S images appears to be light transmission through some of the particles. Figure 11c shows examples of ice particles with "holes" in them that do not appear to be caused by diffraction of out-of-focus images. Figure 11d shows examples of CPI images where light transmission is clearly evident and also simulations of the same images using a 50% threshold and pixel averaging from 2.3- to 10-μm pixels. The simulations strongly suggest that light transmission may account for some of the holes seen in the images in Fig. 11c. Still another factor that makes automated processing of 2D-S images challenging due to the fast response and high resolution is that diffraction from edge effects can appear as small pieces of particles around an image. An example of this effect is denoted by the arrow in Fig. 11c. Finally, there is the challenge of developing an algorithm to combine two stereo views of an ice particle (see Figs. 4 and 5) into estimates of three-dimensional particle shape and volume.

5. Summary

A new optical imaging instrument, the 2D stereo (2D-S) probe, utilizes two laser beams that cross in the middle of the sample volume. The overlap region where the two laser beams intersect defines an area where two orthogonal views of particles are obtained. An overlap region is defined by the two laser beams, improving the sample volume boundaries and sizing of small ($<\sim$100 μm) particles, compared to conventional optical array probes. Results from initial laboratory and flight tests show that the 2D-S is capable of recording particle images with 10-μm pixel resolution at jet aircraft speeds. The stereo views of particles in the overlap region can also improve determination of the three-dimensional shape of a particle.

Data collected by three research aircraft are examined and discussed. 2D-S images from flights in upslope, cirrus, and wave clouds on the SPEC Learjet were compared with 2D-C and CPI images. Particle images were also compared from CPIs installed on the SPEC Learjet and the NASA WB-57 with a 2D-C probe on the Learjet and a CIP probe on the WB-57. Data were collected and compared with FSSP, 2D-C, 260X, and 2D-S probes installed on the NCAR C-130 for the RICO (warm rain) project.

The 10-μm pixel resolution combined with 128 photodiodes that have very fast time response enables the 2D-S to see fine details of ice crystals and small water drops coexisting in mixed-phase clouds. That is, 10–30-μm-diameter cloud drops can be seen within the same field of view along with an ice crystal that has a size of several hundreds of microns. The 2D-S sees thousands of particles $<\sim$150 μm when the 2D-C and 260X see few or none. The 2D-S installed on a Learjet detected $\approx$50 μm ice crystals in the mixed-phase region of a wave cloud approximately 1 km upwind of the 2D-C probe, which did not detect ice particles until they reached sizes of about 200 μm. The shapes of ice particles observed by the 2D-S agreed fairly well with the CPI, which reveals the detailed structure of ice particles due to its 2.3-μm resolution and 256 gray levels.

Measurements in warm cumuli collected by the NCAR C-130 during the RICO project provided an excellent test bed to compare the 2D-S with the NCAR 2D-C and 260X probes. Regions of cloud were selected where the drop diameters, determined by visual analysis of in-focus 2D-S images, did not exceed a specified value. The data showed that the 2D-C and 260X probes recorded a very small fraction (about 0.1%) of images with diameters from about 30 to 150 μm that were seen by the 2D-S and none of the images $<\approx$100 μm.

Overall, the results presented here suggest that historical particle size distributions $<\approx$150 μm collected at $>$100 m s^{-1} by the 2D-C are probably (erroneously) generated from particles $>$150 μm that appear smaller due to inadequate time response. To some extent the same conclusion may be true for data collected with some of the DMT CIP probes. However, as pointed out in a footnote in this paper, the CIP probe has been recently upgraded with a new photodiode array, and
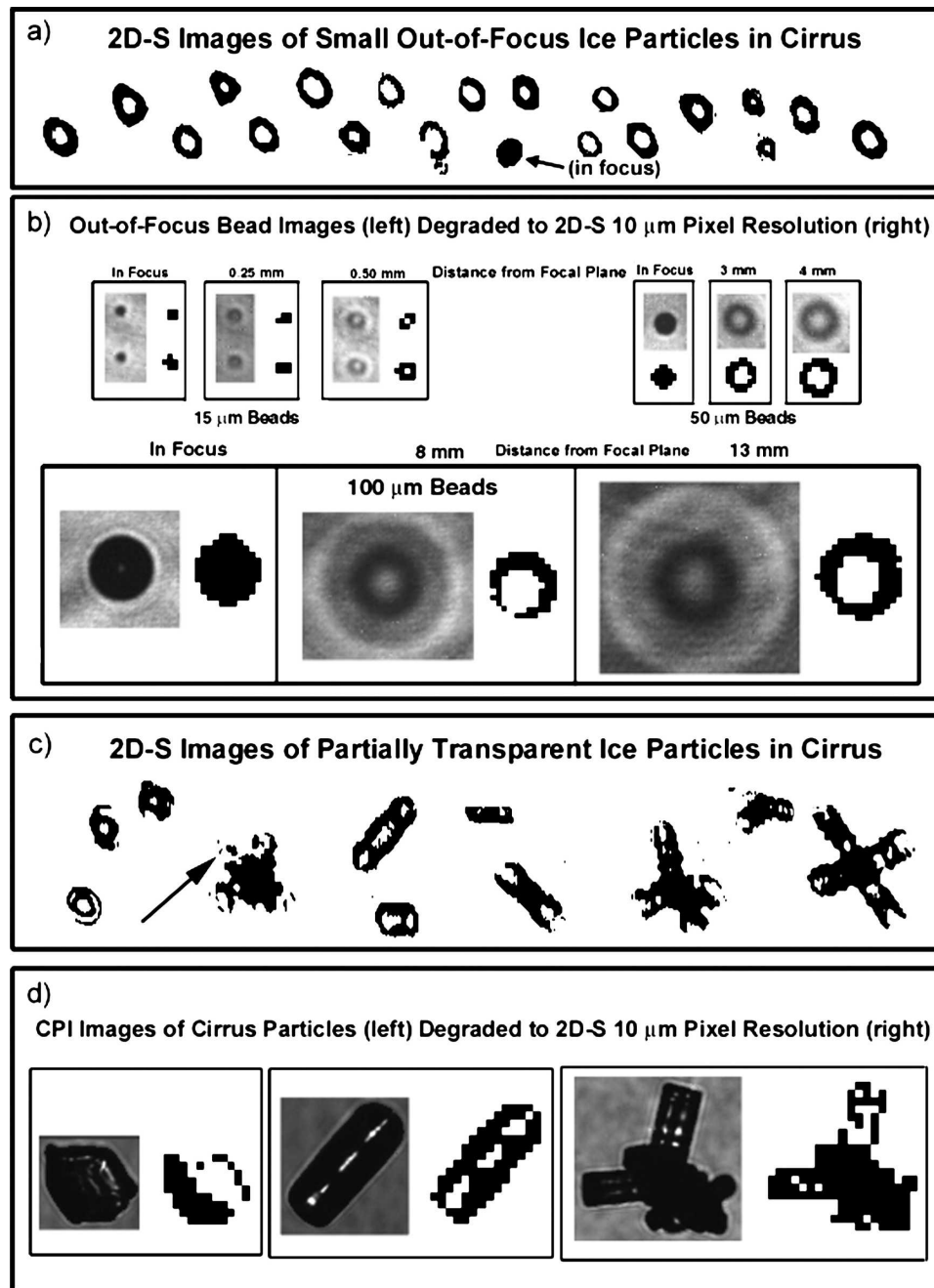
FIG. 11. Examples of (a) out-of-focus, mostly spherical 2D-S images collected in cirrus and (b) images of glass beads taken with the 2D-S in the laboratory where a linear array has been replaced by a digital camera. The glass beads are positioned at various locations from the focal plane (shown in mm above the images), and simulations of equivalent 2D-S images using a 50% threshold and 10-μm pixel resolution are shown to the right of each image. Examples are also shown of (c) 2D-S images of cirrus ice particles where the holes in the ice particles could be due to light transmission through the particles, and (d) CPI images of ice particles where light transmission is apparent. Shown to the right of each CPI image in (d) is a simulation of equivalent 2D-S images using a 50% threshold and averaging the 2.3-μm CPI pixels to 10 μm.

theoretically its time response should now fall somewhere between that of the 2D-C and 2D-S probes.

While comparison of 2D-S images with other imaging probes points out many advantages of the 2D-S, several challenges remain before 2D-S performance is well characterized and software is developed to take full advantage of the data. In particular, further development is needed to resize out-of-focus images based on laboratory measurements, eliminate artifacts from edge diffraction of some out-of-focus particles, reliably determine stereo particles using automated software, and reconstruct three-dimensional shape from two stereo views of a particle.

REFERENCES

Baker, B. A., and R. P. Lawson, 2006: In situ observations of the microphysical properties of wave, cirrus and anvil clouds. Part I: Wave clouds. *J. Atmos. Sci.,* in press.

Baumgardner, D., and A. Korolev, 1997: Airspeed corrections for optical array probe sample volumes. *J. Atmos. Oceanic Technol.,* **14,** 1224–1229.

——, H. Jonsson, W. Dawson, D. O'Connor, and R. Newton, 2001: The cloud, aerosol and precipitation spectrometer: A new instrument for cloud investigations. *Atmos. Res.,* **59-60,** 251–264.

Blyth, A. K., S. Lasher-Trapp, A. Cooper, C. Knight, and J. Latham, 2003: The role of giant and ultra-giant nuclei in the formation of early radar echoes in warm cumulus clouds. *J. Atmos. Sci.,* **60,** 2557–2572.

Cober, S. G., G. A. Isaac, and A. V. Korolev, 2001: Assessing the Rosemount icing detector with in situ measurements. *J. Atmos. Oceanic Technol.,* **18,** 515–528.

Gayet, J.-F., P. R. Brown, and F. Albers, 1993: A comparison on in-cloud measurements obtained with six PMS 2D-C probes. *J. Atmos. Ocean. Technol.,* **10,** 180–194.

——, and Coauthors, 2002: Quantitative measurement of the microphysical and optical properties of cirrus clouds with four different in situ probes: Evidence of small ice crystals. *Geophys. Res. Lett.,* **29,** 2230–2233.

Jensen, J. B., and H. Granek, 2002: Optoelectronic simulation of the PMS 260X optical array probe and application to drizzle in a marine stratocumulus. *J. Atmos. Oceanic Technol.,* **19,** 568–585.

Knollenberg, R. G., 1970: The optical array: An alternative to scattering or extinction for airborne particle size determination. *J. Appl. Meteor.,* **9,** 86–103.

——, 1981: Techniques for probing cloud microstructure. *Clouds, Their Formation, Optical Properties, and Effects,* P.V. Hobbs and A. Deepak, Eds., Academic Press, 15–91.

Korolev, A. V., 2005: Retrieval of sizes of spherical particles from their shadow images. Final Rep. to SPEC Incorporated, 54 pp. [Available online at http://www.specinc.com/publications/A_2D-S_Report.pdf.]

——, 2006: Reconstruction of the sizes of spherical particles from their shadow images. Part I: Theoretical considerations. *J. Atmos. Oceanic Technol.,* in press.

——, S. V. Kuznetsov, Y. E. Makarov, and V. S. Novikov, 1991: Evaluation of measurements of particle size and sample area from optical array probes. *J. Atmos. Oceanic Technol.,* **8,** 514–522.

——, J. W. Strapp, and G. A. Isaac, 1998: Evaluation of the accuracy of PMS optical array probes. *J. Atmos. Oceanic Technol.,* **15,** 708–720.

Lawson, R. P., and R. H. Cormack, 1995: Theoretical design and preliminary tests of two new particle spectrometers for cloud microphysics research. *Atmos. Res.,* **35,** 315–348.

——, B. A. Baker, C. G. Schmitt, and T. L. Jensen, 2001: An overview of microphysical properties of Arctic clouds observed in May and July during FIRE.ACE. *J. Geophys. Res.,* **106,** 14 989–15 014.

——, ——, Q. Mo, and B. Pilson, 2006: In situ observations of the microphysical properties of wave, cirrus and anvil clouds. Part II: Cirrus clouds. *J. Atmos. Sci.,* in press.

Mazin, I. P., A. V. Korolev, A. Heymsfield, G. A. Isaac, and S. G. Cober, 2001: Thermodynamics of icing cylinder for measurements of liquid water content in supercooled clouds. *J. Atmos. Oceanic Technol.,* **18,** 529–542.

NCAR, 2003: Standard output data products from the NCAR Research Aviation Facility. Bulletin No. 9. [Available online at http://raf.atd.ucar.edu/Bulletins/bulletin9.html.]

Strapp, J. W., F. Albers, A. Reuter, A. V. Korolev, U. Maixner, E. Rashke, and Z. Vukovic, 2001: Laboratory measurements of the response of a PMS OAP-2DC. *J. Atmos. Oceanic Technol.,* **18,** 1150–1170.